# Pressure-temperature diagram of wetting and dewetting in a hydrophobic grain boundary and the liquidlike to icelike transition of monolayer water

Meng Chen,[1,*] Huijun Zhou,[1,2] Runliang Zhu,[1] and Hongping He[1,2]

[1]*CAS Key Laboratory of Mineralogy and Metallogeny, Guangdong Provincial Key Laboratory of Mineral Physics and Materials, Guangzhou Institute of Geochemistry, Institutions of Earth Science, Chinese Academy of Sciences (CAS), Guangzhou 510640, China*

[2]*University of Chinese Academy of Sciences, Beijing 100049, China*

(Received 7 January 2020; revised manuscript received 7 April 2020; accepted 7 April 2020; published 27 April 2020)

In coexistence with bulk water, wetting in the hydrophobic grain boundary is unavailable at ambient conditions, because of less energy gain when water is on top of a hydrophobic surface. However, this study discloses a high-pressure driven wetting between hydrophobic surfaces. The dewetting-wetting transition pressure is higher when temperature increases, due to a competition between enthalpy gain and entropy loss. The stably wetting water monolayer exhibits a continuous phase transition from a liquidlike to a square-ice-like form, through interconversions between liquid and square-ice components. The diagram of dewetting-wetting and liquidlike-icelike transitions is delivered here.

DOI: 10.1103/PhysRevB.101.165432

## I. INTRODUCTION

Wettability of water on a solid surface influences residence and transportation of water in the solid matrix, playing a key role in the water cycle from the Earth's surface to the interior [1–3]. Whether a solid surface is hydrophobic or hydrophilic is judged by the contact angle of a water droplet on top of it [4]. The contact angle is determined by interfacial tensions of solid/vapor, solid/water, and water/vapor interfaces, according to the Young's equation. As for a solid grain boundary in coexistence with bulk water in a hydrostatic condition [Fig. 1(a)], the grain and bulk water are under the same pressure $p_{\mathrm{coex}}$, which is the same as the perpendicular pressure $p_\sigma$ across the boundary. If $N$ water molecules stably wet the boundary, the conditions $p_\sigma = p_L = p_{\mathrm{coex}}$ and $\mu(N) = \mu_{\mathrm{coex}}$ are fulfilled [5]. $p_L$ is the lateral pressure of the grain boundary, while $\mu(N)$ and $\mu_{\mathrm{coex}}$ are chemical potentials of water in the boundary and bulk water. If $\Delta N$ water molecules are added into the grain boundary, it introduces an external force, namely, disjoining pressure $\Pi = p_\sigma - p_L$ [6]. On the other hand, it also causes a variation in chemical potential $\Delta\mu = \mu(N + \Delta N) - \mu_{\mathrm{coex}}$. The hydration Gibbs free energy $\Delta G_{\mathrm{hyd}}$ is introduced [7]:

$$\Delta G_{\mathrm{hyd}}(N) = \int_0^N [\mu(N') - \mu_{\mathrm{coex}}]dN', \tag{1}$$

or

$$\Delta G_{\mathrm{hyd}}(L) = -A\int_0^L \Pi(N')dL', \tag{2}$$

where $A$ is the boundary surface area and $L$ is the confining distance of the boundary. Apparently, the minimum of $\Delta G_{\mathrm{hyd}}$ corresponds to $\Pi = 0$ and $\mu(N) = \mu_{\mathrm{coex}}$, which characterizes the stable coexistence state.

Although hydrations in the grain boundary and on a solid/vapor surface are different situations, Kanduč *et al.* showed there is a quantitative correlation [8,9]. If two surfaces are hydrophobic, as characterized by a large contact angle of a water droplet on top, hydration between such two surfaces is unavailable. $\Delta G_{\mathrm{hyd}}$ can be decomposed as $\Delta G_{\mathrm{hyd}} = \Delta U - T\Delta S + p\Delta V$. The $p\Delta V$ term makes a significant contribution to capillary condensation of gas molecules because of the large $\Delta V$ [10]. However, in the ambient conditions both $p$ and $\Delta V$ of bulk water are small, so that $p\Delta V$ is negligible. Thence, ambient hydration just depends on the competition between energy gain and entropy loss. A well-developed hydrogen bonding network connecting water and a surface, which is the characteristic of most hydrophilic surfaces [11,12], contributes to the potential energy gain and drives hydration. However, in the high-pressure (several GPa) regime due to the enhancement of $p$, the $p\Delta V$ term becomes significant, and thus wetting in the grain boundary might not necessarily require a large energy gain. Our recent study disclosed a high $p\Delta V$ term drives hydration in hydrophobic interlayers of phyllosilicate minerals with the coexistence of bulk water [13]. As to disclose if wetting in the grain boundary under several GPa is a common phenomenon, water confined between structureless hydrophobic surfaces needs to be studied primarily. Structureless surfaces act as models of hydrophobic surfaces and help to distinguish between influences of surface and surface atomic structure [14,15].

This study, with thermodynamic integrations (TIs) based on molecular dynamics (MD) simulations, will show at a fixed temperature ($T$), wetting in a structureless hydrophobic grain boundary with the coexistence of bulk water is available when

*chenmeng@gig.ac.cn

 

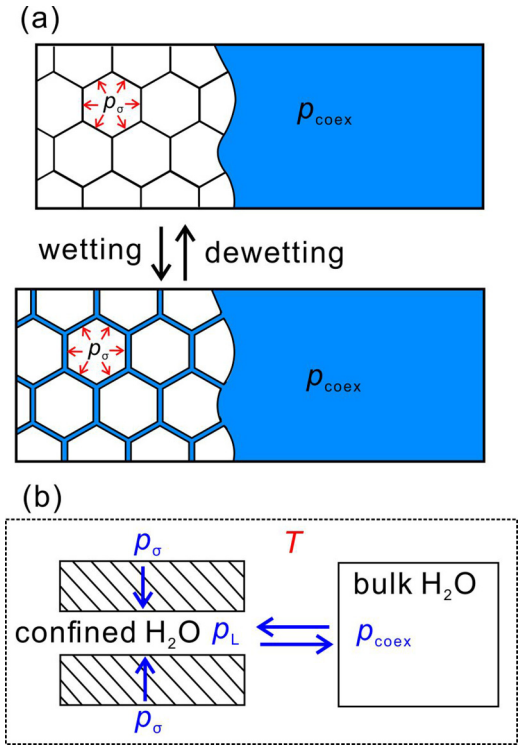


FIG. 1. (a) Schematic of dewetting-wetting in the grain boundary. (b) The coupling between confined water and bulk water under the coexistence pressure and temperature.

pressure ($p_{coex}$) is high enough. The stably wetting form is transformed from a liquidlike to an icelike monolayer as $p_{coex}$ increases. The icelike monolayer exhibits the form similar to the widely reported square ice [16–18]. Previous simulations disclosing square ice were with different settings, and they are as follows: (1) The confining spacing is constrained and water density is fixed or coupled to a lateral pressure [17,18]; (2) a fixed number of water molecules are confined in flexible confining walls in vacuum [19]; (3) water is confined in flexible confining walls in vacuum and it is coupled to bulk water under a high external pressure [16,20]. Thus, no simulation result could well answer the following question: Is square ice a thermodynamically stable wetting form when the confinement and the coupling bulk phase are under the coexistence $p-T$ condition? This question will be well answered here. The results shed light on understanding how water resides in the Earth's interior and the transportation form of water [21–23].

## II. METHODOLOGY

### A. Simulation details

Models of water confined between walls were built. The TIP4P/2005 force field [24] was used to describe water, because it well delivers the phase diagram of water [24–26]. The water-wall interactions were described by a Lennard-Jones potential: $U_{LJ} = 4\pi\varepsilon[(\sigma/r)^{12} - (\sigma/r)^6]$, where $\varepsilon$ and $\sigma$ for interactions between a wall site and a water O atom were 0.831 kJ/mol and 0.316 nm, respectively, while those between a wall site and a water H atom were 0.415 kJ/mol and 0.284 nm, respectively [17]. These parameters mimic the van der Waals interactions between a silica grain and water. The density of wall interaction sites was set to 80 $nm^{-3}$, which is more or less the density of Si and O atoms in silica. The integration over the interaction sites with a 12-6 potential delivers a 9-3 potential form. The Lennard-Jones potential was smoothly switched off from 1.0 to 1.2 nm. Periodic boundary conditions were applied in the $xy$ plane. The particle-mesh Ewald (PME) method [27,28] was used to calculate long-range electrostatic interactions between water molecules. As the system has a slab geometry in the $xy$ plane, the $z$ dimension of the box was scaled by 3 for Ewald summation so as to decrease the unphysical Coulomb interaction between periodic images. A force and potential correction was applied in the $z$ dimension to produce a pseudo-two-dimensional summation. The relative dielectric constant of the wall is 1.

Extensive MD simulations on different numbers ($N$) of confined water under different temperature ($T$) and pressure ($p_\sigma$) conditions were performed. $N$ ranged from 1 to 150. The interval of $N$ was 1 in the range $1 \leqslant N \leqslant 10$, while it was 10 for $N > 10$. A model with $N$ water molecules confined between walls was simulated in isothermal-isobaric (*NPT*) and canonical (*NVT*) ensembles sequentially for 100 ps and 5 ns, respectively. Temperature was coupled with the velocity rescaling thermostat [29], while pressure was with the Berendsen barostat [30]. The Berendsen instead of Parrinello-Rahman method [31,32] was used here, because the latter would lead to large volume fluctuations especially when $N$ is small. Only the $z$ dimension was scaled in the *NPT* run, so that it was an $NP_zT$ run exactly. Coupling temperatures ($T$) ranged from 400 to 900 K with an interval of 50 K. Coupling pressures ($p_\sigma^*$) in $NP_zT$ runs ranged from 0.4 to 6 GPa when $T \leqslant 600$ K, and at higher temperatures they ranged from 0.4 to 8 GPa. The pressure interval is 0.2 GPa. Because the Berendsen barostat does not produce the exact *NPT* ensemble, the $NP_zT$ run is just utilized to achieve approximate equilibrium configurations, but data collection is through the *NVT* run. Evolutions of potential energy and $p_\sigma$ of *NVT* runs with time show equilibrium configurations are achieved during the simulation time (Figs. S1 and S2 in the Supplemental Material (SM) [33]). In some systems (Fig. S2(d) in the SM [33]), spontaneous drops of potential energy and $p_\sigma$ can be seen, because of the reorganization into a square-ice-like structure, which has been shown to be an activated process conforming to the classical nucleation theory [34]. The equilibrium pressure $p_\sigma$ in the $z$ dimension is calculated as the average over the equilibrium *NVT* run, which could deviate a little from the coupling pressure $p_\sigma^*$ in the $NP_zT$ stage. The equilibrium energies, densities, molar volumes, and structural parameters of confined water are also derived through *NVT* runs. Thus, the correspondences between $p_\sigma$, $T$, $N$, and properties of confined water are achieved.

Simulations of a bulk water phase with more than 800 molecules are also performed under the same temperature range (400–900 K) as confined water. The bulk water phase is run for 5 ns in an *NPT* ensemble with a simulation pressure of 0.4 GPa. Thence, the equilibrium configuration is utilized to initiate a series of simulations under consecutive pressures with an interval of 0.2 GPa. The pressure range is consistent with that of simulations of confined water. Those simulations are in an *NPT* ensemble and last for 500 ps each, in which

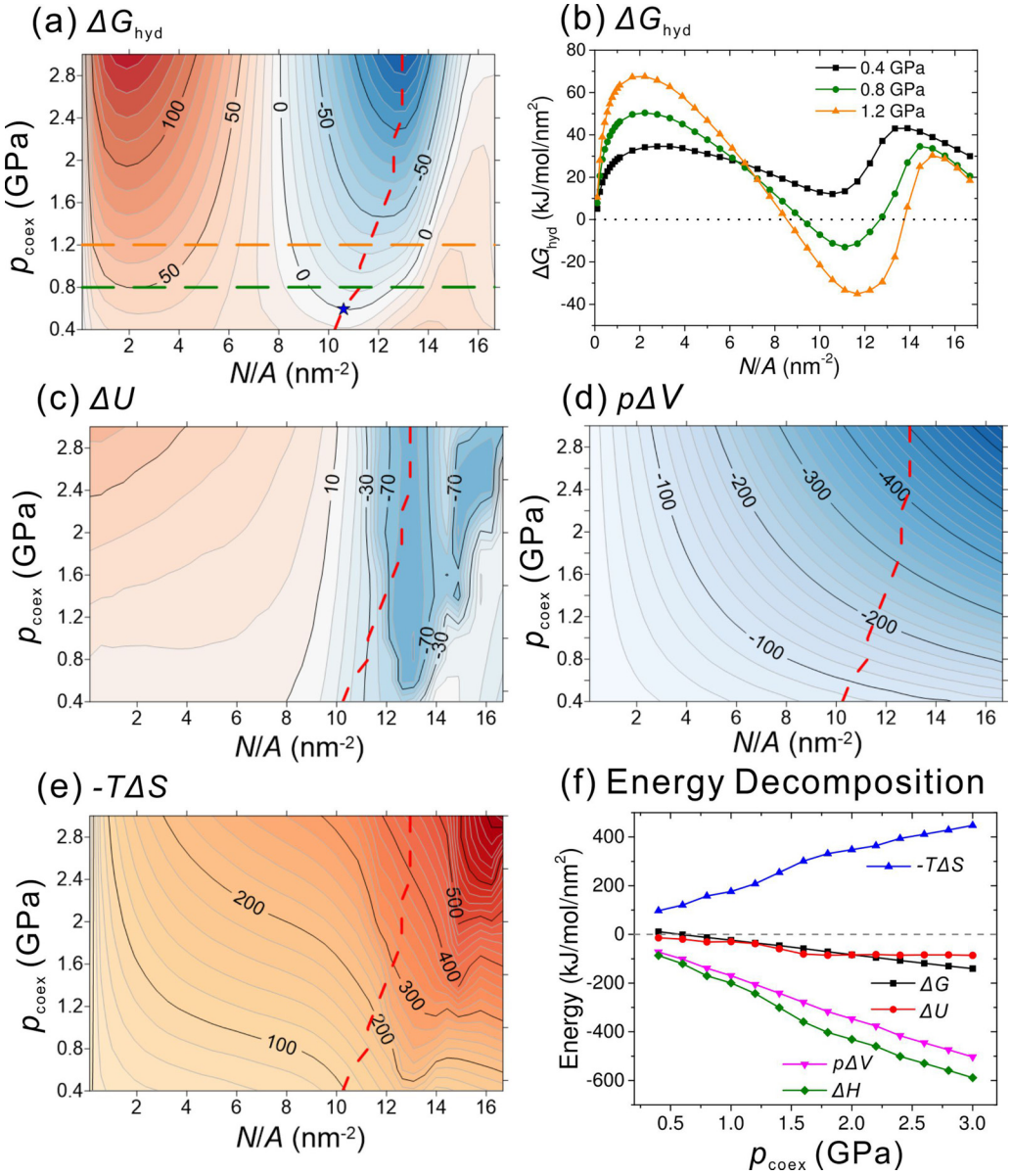


FIG. 2. Energy surfaces of $\Delta G_{\rm hyd}(p_{\rm coex}, N)$, $\Delta U(p_{\rm coex}, N)$, $p\Delta V(p_{\rm coex}, N)$, and $-T\Delta S(p_{\rm coex}, N)$ at $T = 400$ K, as exhibited in panels (a), (c), (d), and (e), respectively. $N$ is normalized by the surface area $A$. The energy unit is kJ/mol/nm$^2$. The cross sections of $\Delta G_{\rm hyd}(p_{\rm coex}, N)$ in panel (a) at $p_{\rm coex} = 0.4$, 0.8, and 1.2 GPa, respectively, are shown in panel (b) and denoted by lines of the same colors. The red dashed line in panels (a), (c), (d), and (e) indicates positions of local minima of $\Delta G_{\rm hyd}$. The star in (a) represents the dewetting-wetting transition point. Panel (f) shows energy terms along the local minima of $\Delta G_{\rm hyd}$ as a function of $p_{\rm coex}$.

the last 300-ps run is used to derive equilibrium properties. Evolutions of potential energy and volume of bulk water with time show that well equilibrated structure is achieved during the simulation time (Fig. S3 in the SM [33]). Temperature and pressure are coupled with the Nosé-Hoover thermostat [35,36] and the Parrinello-Rahman barostat [31,32], respectively.

### B. Chemical potential calculations

Equilibrium configurations of water confined between walls under $p_0$, $T$ conditions were used to initiate stochastic dynamics simulations, which served for the TI procedures so as to derive the chemical potential $\mu(p_0, T, N)$ (Sec. S2 of the SM [33]) [37,38]. $p_0$ was the smallest equilibrium pressure in the $z$ dimension under each $T$ condition, as derived from equilibrium simulations. Thence, the chemical potential under an arbitrary pressure $p_\sigma$ was derived with the following equation:

$$\mu(p_\sigma, T, N) - \mu(p_0, T, N) = \int_{p_0}^{p_\sigma} \left(\frac{\partial V}{\partial N}\right)_{p'_\sigma, T, N} dp'_\sigma, \quad (3)$$

in which $(\frac{\partial V}{\partial N})_{p'_\sigma, T, N}$ was calculated based on equilibrium configurations with different $N$. Similarly, the chemical potential of the coexisting bulk water $\mu_{\rm coex}(p_{\rm coex}, T)$ was also derived with the TI procedures based on extensive simulations. It is noted that under these conditions bulk TIP4P/2005 water remains a liquid phase [26]. After knowing $\mu(p_\sigma, T, N)$ and

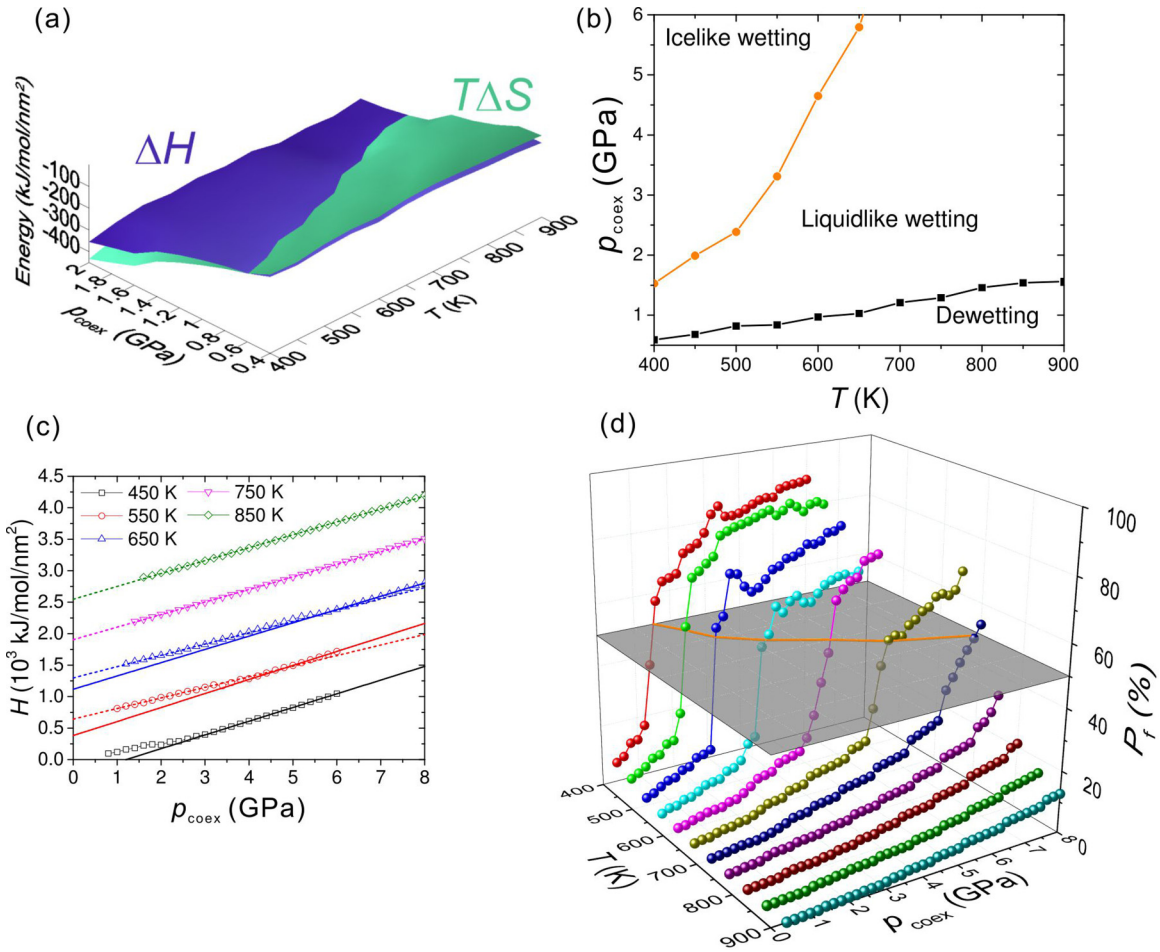


FIG. 3. (a) Energy surfaces of $\Delta H(p_{\text{coex}}, T)$ and $T\Delta S(p_{\text{coex}}, T)$. (b) Diagram of dewetting-wetting and icelike-liquidlike transitions in the grain boundary. (c) Enthalpy of water stably confined in the grain boundary. Enthalpy data have been offset for clarity. Data under other temperature conditions are seen in Fig. S5 of the SM [33]. (d) Ratios ($P_{\text{f}}$) of icelike water molecules as a function of pressure at fixed temperatures. The crossing of $P_{\text{f}}(p_{\text{coex}}, T)$ functions and the $P_{\text{f}} = 50\%$ surface is shown with the orange line.

$\mu_{\text{coex}}(p_{\text{coex}}, T)$, the hydration free energy $\Delta G_{\text{hyd}}(p_{\text{coex}}, T, N)$ under the coexistence pressure and temperature conditions can be derived with Eq. (1).

## III. RESULTS AND DISCUSSIONS

### A. Wetting in the grain boundary

The free energy surface of $\Delta G_{\text{hyd}}(p_{\text{coex}}, T, N)$ at $T = 400$ K [Fig. 2(a)] presents a valley with negative $\Delta G_{\text{hyd}}$, which indicates a thermodynamically favorable wetting regime. With increasing pressure, the local minimum of $\Delta G_{\text{hyd}}$, which is positive when $p_{\text{coex}}$ is small, decreases and becomes negative when $p_{\text{coex}}$ is larger than ca. 0.6 GPa [Figs. 2(a) and 2(b)]. The negative global minima of $\Delta G_{\text{hyd}}$ unambiguously identify the stably wetting states of water in the grain boundary at different pressures. Along the local minima of $\Delta G_{\text{hyd}}$ [the dashed red line in Fig 2(a)], the numeral density of water molecules per surface area ($N/A$) increases gently with pressure.

Wetting in a grain boundary can be imagined as a two-stage process: The first stage is an isothermal-isobaric expansion of grains, during which the free energy does not change because $dG = -SdT + Vdp$ and $T$ and $p$ are constants; second, water molecules from the bulk phase enter the expanded boundary between grains. Thus, the wetting mechanism can be disclosed through decompositions of $\Delta G_{\text{hyd}}(p_{\text{coex}}, T, N)$ into $\Delta U(p_{\text{coex}}, T, N)$, $p\Delta V(p_{\text{coex}}, T, N)$, and $-T\Delta S(p_{\text{coex}}, T, N)$ terms in the second stage [Figs. 2(c)–2(f)]. $\Delta U$ accounts for the internal energy difference between the same $N$ water molecules in confinement and in the bulk phase, as derived through equilibrium simulations. It is negative along the local minima of $\Delta G_{\text{hyd}}$ [Figs. 2(c) and 2(f)], implying wetting in the grain boundary is energetically available. $p\Delta V$ is the volume of $N$ water molecules in the bulk phase multiplied by $-p_{\text{coex}}$. The $-T\Delta S$ term accounts for the contribution of entropy penalty when water is confined, and it is derived through subtracting $\Delta U$ and $p\Delta V$ from $\Delta G_{\text{hyd}}$. $p\Delta V$ and $-T\Delta S$ terms play opposite roles [Figs. 2(d)–2(f)]. The former drives wetting while the latter retards it. At a fixed temperature, the increase of pressure on one hand enlarges the $p\Delta V$ term, and on the other hand enhances the entropy penalty [Fig. 2(f)]. The enthalpy contribution ($\Delta H$, the sum of $\Delta U$ and $p\Delta V$) dominates at an elevated pressure and thus wetting becomes thermodynamically available.

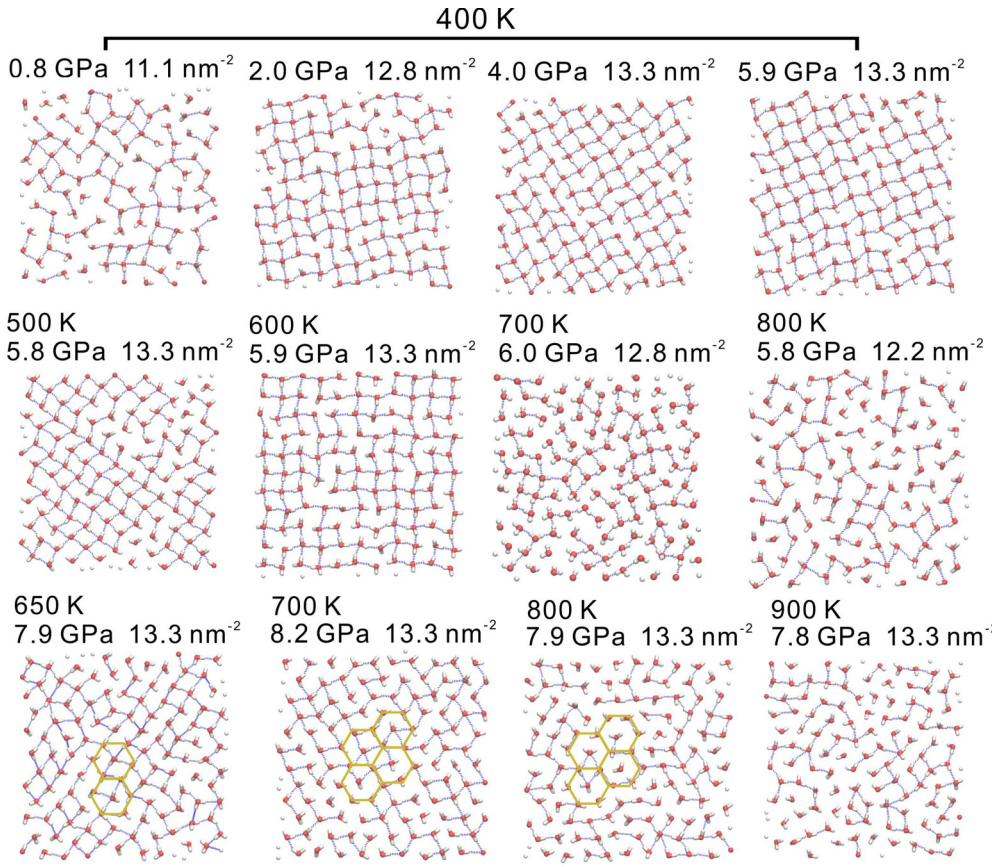


FIG. 4. Snapshots of equilibrium arrangements of confined water. Temperature, equilibrium pressure, and numeral density of water molecules per surface area are marked.

$\Delta G_{\mathrm{hyd}}(p_{\mathrm{coex}}, T, N)$ at other temperatures in the range from 400 to 900 K are exhibited in Fig. S4 of the SM [33]. They all show that wetting in the grain boundary is available when pressure is high enough. Through extracting $\Delta H(N)$ and $T\Delta S(N)$ corresponding to the local minima of $\Delta G_{\mathrm{hyd}}(N)$ at different $p-T$ conditions, energy surfaces of $\Delta H(p_{\mathrm{coex}}, T)$ and $T\Delta S(p_{\mathrm{coex}}, T)$ are built [Fig. 3(a)]. The crossing of energy surfaces of $\Delta H(p_{\mathrm{coex}}, T)$ and $T\Delta S(p_{\mathrm{coex}}, T)$ clearly shows the $p-T$ boundary of the dewetting-wetting transition, as also illustrated in the diagram of Fig. 3(b). Through linearly fitting the $p-T$ boundary, a maximum residue of 0.06 GPa is found. It implies a small uncertainty, which cannot obscure the trend of the boundary. The enthalpy contribution is dominated at a higher pressure [Fig. 3(a)], mainly due to the elevated pressure-volume term. On the other hand, the entropy contribution is enhanced at a higher temperature [Fig. 3(a)]. The opposite roles played by pressure and temperature give rise to the $p-T$ boundary [Fig. 3(b)] which lies at a higher pressure when temperature increases.

### B. Liquidlike-icelike transition

Snapshots of the water monolayer in the grain boundary, which is in the stable wetting state upon the coexistence of bulk water, are extracted (Fig. 4). Snapshots at 400 K show that the monolayer transforms from a disordered liquidlike state into an ordered icelike state with increasing pressure (the top panels in Fig. 4). In the icelike water monolayer, water molecules construct a network mainly consisting of four-membered rings through hydrogen bonds (HBs). This structure is similar to that of the widely reported two-dimensional square ice [16–18], which is an analog of three-dimensional ice VII [19]. Snapshots of the wetting monolayer at other temperatures exhibit icelike ordered or liquidlike disordered structure, depending on temperature and pressure (Fig. 4).

Enthalpy of the stable wetting monolayer as functions of $p_{\mathrm{coex}}$ at different $T$ conditions is calculated [Fig. 3(c)]. Linear fits to isothermal enthalpy curves of relatively lower temperatures ($400-650$ K) show a two-stage variation of enthalpy with pressure (Fig. 3(c), and Fig. S5 in the SM [33]), implying a phase transition. However, no sharp drop or elevation of enthalpy as pressure increases is observed, such that it is probably not a first-order but a continuous (second-order) transition. Han *et al.* have shown, at a fixed confining distance, above 250 K the monolayer liquid–square-ice transition with water density is continuous as evidenced by a continuous variation of structure [18]. The settings here are different from those of Han *et al.*, as we allow the confining distance to vary with pressure and the investigated water monolayer is a stably wetting form coupled to bulk water. We clearly show that under certain temperatures, the stably wetting monolayer undergoes a continuous phase transition as pressure increases.

On the other hand, at higher temperatures 750 − 900 K), the enthalpy curve is nearly linear in the studied pressure range ( Fig. 3(c), and Fig. S5 in the SM [33]). Thus in this regime, no phase transition is available. Snapshots (Fig. 4) show the water monolayer at 800 − 900 K does not well develop square-ice-like structure and remains a liquidlike state even when pressure is as high as ca. 8.0 GPa.

The icelike monolayer is different from ice because of the lack of a complete long-range order, as shown by defects in the HB network even under ca. 6.0 GPa at 400 K (Fig. 4). Water molecules around the defects of the HB network are seen as disordered water molecules. It was argued that a long-range crystalline order in two-dimensional systems is unavailable [39,40]. Previous simulation studies also showed monolayer square ice confined between graphene sheets bears defects or is just a nanoscale object, lacking a long-range order [19,34]. On the other hand, even in the liquidlike water monolayer, four-membered rings, which are the structural components of square ice, are still present, although they do not dominate. Either a liquidlike or icelike water monolayer shown here can be seen as a mixture of liquid and square-ice components. As to quantify the liquidlike or icelike extent, the ratio ($P_f$) of water molecules participating in four-membered rings is calculated:

$$P_f = \sum_{i=0}^{N} n_i/4, \tag{4}$$

where $n_i$ is the number of four-membered rings a water molecule participates in, which is determined according to the HB criterion: the donor-acceptor distance, the hydrogen-acceptor distance, and the hydrogen-donor-acceptor angle are less than 0.35 nm, 0.245 nm, and 30°, respectively [41,42]. A sharp but seemingly continuous increase of $P_f$ with pressure is observed for the temperature range 400−700 K [Fig. 3(d)]. From a structural point of view, a discrete or continuous variation of an order parameter distinguishes between first-order and second-order (continuous) phase transitions. However, due to the discrete data set, the sharp increment of $P_f$ between some adjacent pressure conditions might make it hard to determine the phase transition order. In a two-component system, if a phase transition is continuous, the state with an equal fraction of two alternative components can be found and it corresponds to the phase transition point [43]. For $P_f$ ($p$) isotherms at 400, 450, 500, 550, 600, and 650 K, points of $P_f$ equal to 57.3%, 51.1%, 53.9%, 51.6%, 45.9%, and 50.3% can be found, respectively [Fig. 3(d)]. Although the exact data of $P_f = 50\%$ which can unambiguously determine a continuous transition are missing, those data close to 50% indicate the transition is probably a continuous one. We use the crossing of $P_f(p)$ isotherms and the $P_f = 50\%$ surface to determine the phase transition line [Fig. 3(b)]. The phase transition line almost coincides with inflection points of the enthalpy curves [Fig. 3(c), and Fig. S5 in the SM [33]). Since the pressure interval is more or less 0.2 GPa, the uncertainty would be less than it. Thus, a second-order transition between liquidlike and icelike water monolayers through interconversions between liquid and square-ice components is evidenced.

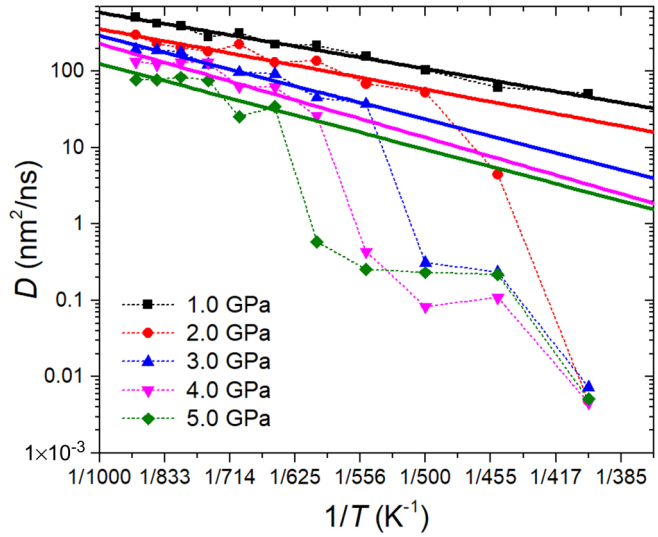


FIG. 5. Diffusion coefficients of the stably wetting water. The pressure denotes the initial coupling pressure $p_\sigma^*$ during the $NP_zT$ run. Solid lines show the exponential fits to diffusion coefficients.

The influence of the liquidlike-icelike transition on water dynamics is disclosed through calculating the diffusion coefficients ($D$). The systems more or less corresponding to the stable wetting states are considered. As icelike water diffuses slowly, the $NVT$ simulation time of the investigated systems is extended to 30 ns. $D$ is derived through linearly fitting the mean square displacements with the Einstein equation: $\frac{1}{N}\sum_{i=1}^{N}|\vec{r_i}(t) - \vec{r_i}(0)|^2 = 2dDt$, in which $\vec{r_i}(t)$ is the displacement vector of a water O atom at time $t$ and $d$ is the dimension. Since only two-dimensional displacements are considered, $d$ is 2. Across the liquidlike-icelike transition, a two-stage dependence of $D$ on temperature is shown (Fig. 5). In the liquidlike regime, the decay of $D$ with inverse $T$ approximately follows the Arrhenius law [44], as shown by the exponential fit. The data fluctuation around the exponential fit might be caused by those results not being exactly under the same pressure conditions. Since $NVT$ simulations are performed after $NP_zT$ ones the equilibrium pressure $p_\sigma$ could deviate slightly from the initial coupling pressure $p_\sigma^*$. $D$ drops significantly across the liquidlike-icelike transition, because icelike water rarely diffuses and a translational motion requires the breakage of the adjacent HB network.

This liquidlike-icelike transition of monolayer water recalls the suspected liquid-liquid transition of three-dimensional water across the Widom line [45,46]. Water has been suspected as a mixture consisting of two distinct components, i.e., an ordered hydrogen-bonding component and a disordered one, which can be distinguished by local order parameters [47–49]. Below or above the Widom line, water is dominated by an alternative component. In the isotherm across the Widom line, with increasing pressure, the fraction of a component experiences a sharp but continuous variation [48]. A two-stage dependence of $D$ of supercooled bulk water on temperature can also be found across the Widom line [50]. These phenomena are similar to the liquidlike-icelike transition of monolayer water, which is also induced by

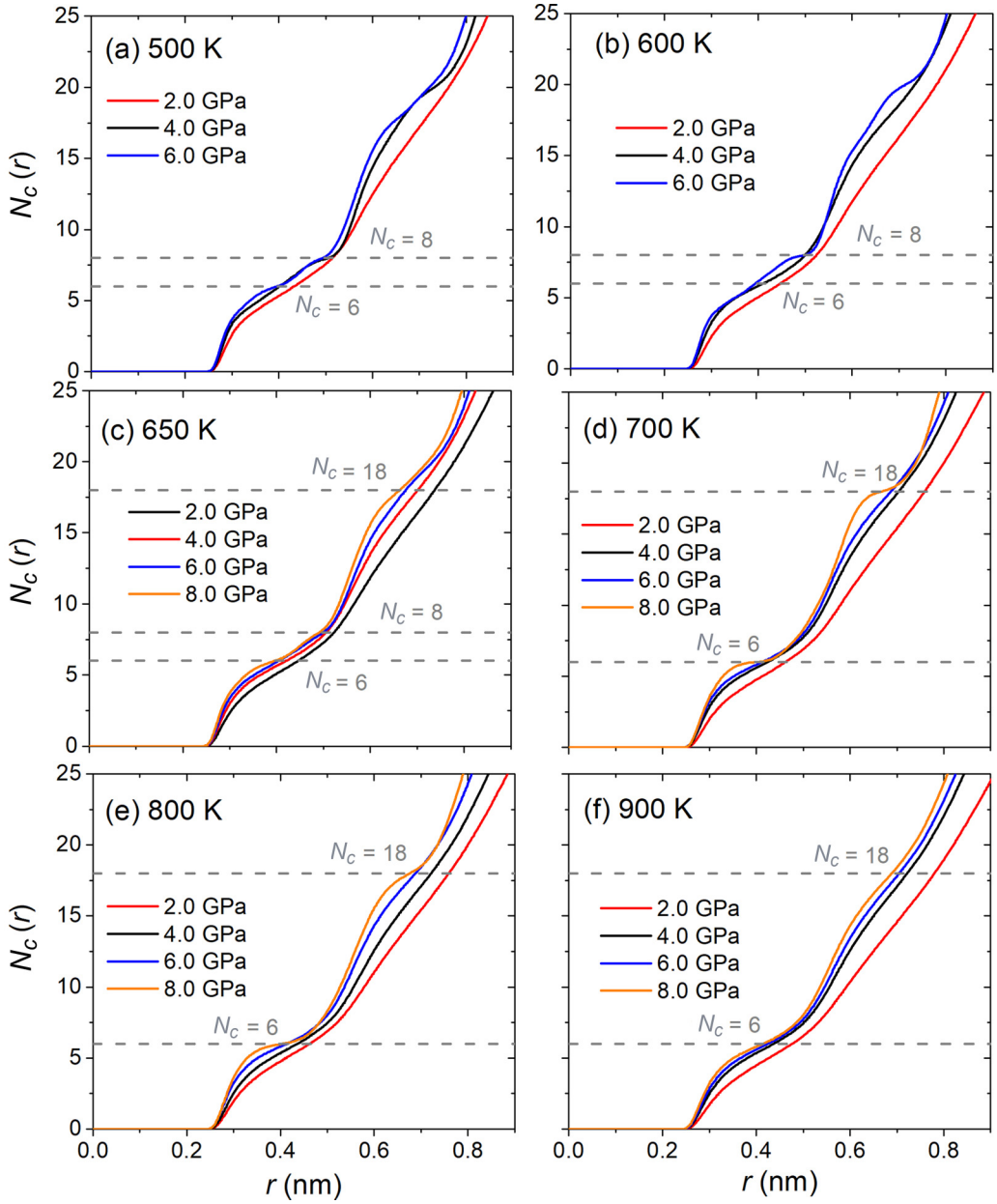


FIG. 6. Coordination numbers $N_C$ $(r)$ between water O atoms. The pressure denotes the initial coupling pressure $p_\sigma^*$ during the $NP_zT$ run.

interconversions between two components, a HB supported ordered component and a disordered one.

### C. Closest-packing water arrangement

Under some high pressure but in the liquidlike regime (at ca. 8 GPa and 700−800 K), a hexagonal closest-packing water arrangement is observed for the wetting monolayer (Fig. 4). This arrangement is similar to that of water intercalated in phyllosilicate minerals also under high pressure [13]. It has also been reported as a hexatic phase [51]. O atoms of water in this hexagonal closest-packing arrangement are long-range ordered, as evidenced by periodic oscillations in the radial distribution functions (RDFs) between them (Fig. S6 in the SM [33]). However, H atoms are disordered. This closest-packing arrangement can be quantified by the coordination numbers ($N_C$) [13] (Fig. 6). For the well-developed long-range closest-packing arrangement, $N_C$ in the two minima of the RDF with radii around 0.40 and 0.67 nm, respectively, are approximately 6 and 18, as shown in cases when $p_\sigma$ is ca. 8 GPa and $T$ is 700 or 800 K [Fig. 6(d) and 6(e)]. As $p_\sigma$ decreases, the steps of $N_C = 6$ or 18 generally disappear, implying the loss of the long-range closest-packing order. When $T$ is as high as 900 K, even under the highest studied pressure, a long-range ordered arrangement is not available (Fig. 4), as there is no obvious step of $N_C = 18$ [Fig. 6(f)]. Probably as temperature increases, the development of such an arrangement requires a higher pressure. When $T$ is 650 K, the local closest-packing arrangement under ca. 8 GPa can be observed (Fig. 4), but a long-range order is lacking, as evidenced by the less obvious steps of $N_C = 6$ and 18 [Fig. 6(c)]. On the other hand, a kink of $N_C = 8$ appears, implying the square-ice structure,

as also found in the snapshot (Fig. 4). When $T$ is 650 K or lower, the development of square-ice structure prohibits the formation of a long-range closest-packing arrangement [Figs. 6(a)–6(c)]. Thus, the development of a long-range ordered closest-packing water monolayer is under conditions where square-ice structure is not well developed. It belongs to the liquidlike phase.

Studies of bulk water beneath the melting curve above 4 GPa showed that water behaves like a common liquid exhibiting a closest-packing structure [52,53]. Thus, the two-dimensional closest-packing liquid water monolayer shown here can be seen as an analog of three-dimensional closest-packing water.

### D. Discussions

Rigid structureless surfaces are utilized here. As we know, flexibility and atomic structure of a surface influence the state of confined water [15,19,54,55]. However, investigating structureless surfaces serves as a prerequisite to show the influences of hydrophobic surfaces without the interference of atomic structure. The structure of water confined between structureless surfaces here is consistent with that between some atomic surfaces. The closest-packing water monolayer has also been found intercalated in phyllosilicate minerals [13]. Square ice has been found in the confinement of graphene sheets [16] or on top of some metal surfaces [15]. Either square ice or closest-packing water is an energetically favored state under certain $p-T$ conditions. Within atomic surfaces, such a state may not be interfered with, or be strengthened, or be transformed into a new energetically favored state. If the atomic surfaces do not form HBs with water, like graphene [16], square-ice-like structure might still be supported. As for atomic surfaces forming HBs with water, such as cristobalite [54] and mica [56], square-icelike structure might not be available but distinct icelike structure is supported. As to the closest-packing arrangement of water, because it matches the arrangement of silicate rings, it is supported in interlayers of phyllosilicate minerals [13]. Nevertheless, one thing is clear: With the coexistence of bulk water, an energetically favored wetting state would be thermodynamically favored when the coexistence pressure is high enough.

Future work would be using the methodology here to investigate the wetting behavior of water in the realistic grain boundaries. It would be interesting to show how the atomic structure of a surface influences the $p-T$ boundary of dewetting-wetting and the phase transition. Understanding the low-dimensional existing state of water in coexistence with bulk water under different $p-T$ conditions gives rise to disclosing the transportation form of water under these conditions. In addition, the icelike confined water might reduce the friction between grains [57], which could impact the slip behavior in the deep Earth.

## IV. CONCLUSIONS

In summary, we disclose that the dewetting-wetting transition in a hydrophobic grain boundary in the coexistence with bulk water is driven by high pressure, and a stably wetting form can be liquidlike or icelike depending on the $p-T$ condition. The transition between liquidlike and icelike water monolayers is continuous, through interconversions between liquid and square-ice components. Square ice can be seen as an analog of three-dimensional high-pressure ice VII. On the other hand, a long-range ordered closest-packing water monolayer appears at certain high-pressure conditions, being an analog of three-dimensional closest-packing water. It belongs to a liquidlike state. With the methodology utilized here, detailed investigations on wetting states between realistic surfaces under high pressure are available.

## ACKNOWLEDGMENTS

This is contribution No. IS-2856 from GIGCAS. This work was financially supported by the Youth Innovation Promotion Association CAS (Grant No. 2019345). We are grateful to the National Supercomputer Center in Guangzhou for the use of the high-performance computing facility.

[1] C. E. Neuzil, Nature **403**, 182 (2000).
[2] M. Faccenda, T. V. Gerya, N. S. Mancktelow, and L. Moresi, Geochem. Geophys. Geosyst. **13**, Q01010 (2012).
[3] K. Mibe, T. Fujii, and A. Yasuda, Nature **401**, 259 (1999).
[4] C. Zhu, H. Li, Y. Huang, X. C. Zeng, and S. Meng, Phys. Rev. Lett. **110**, 126101 (2013).
[5] P. Tarazona, H. Martínez, E. Chacón, and F. Bresme, Phys. Rev. B **85**, 085402 (2012).
[6] R. Evans and U. Marini Bettolo Marconi, J. Chem. Phys. **86**, 7138 (1987).
[7] E. D. Shchukin, A. V. Pertsov, E. A. Amelina, and A. S. Zelenev, *Colloid and Surface Chemistry* (Elsevier, Amsterdam, 2001), Vol. 12.
[8] M. Kanduč and R. R. Netz, Proc. Natl. Acad. Sci. USA **112**, 12338 (2015).
[9] M. Kanduč, A. Schlaich, E. Schneck, and R. R. Netz, Langmuir **32**, 8767 (2016).
[10] R. Evans, J. Phys.: Condens. Matter **2**, 8989 (1990).
[11] J. D. Cyran, M. A. Donovan, D. Vollmer, F. S. Brigiano, S. Pezzotti, D. R. Galimberti, M.-P. Gaigeot, M. Bonn, and E. H. Backus, Proc. Natl. Acad. Sci. USA **116**, 1520 (2019).
[12] A. M. Schrader, J. I. Monroe, R. Sheil, H. A. Dobbs, T. J. Keller, Y. Li, S. Jain, M. S. Shell, J. N. Israelachvili, and S. Han, Proc. Natl. Acad. Sci. USA **115**, 2890 (2018).
[13] M. Chen, H. Zhou, R. Zhu, X. Lu, and H. He, Langmuir **36**, 618 (2020).
[14] J. Bai, C. A. Angell, and X. C. Zeng, Proc. Natl. Acad. Sci. USA **107**, 5718 (2010).
[15] C. Zhu, Y. Gao, W. Zhu, J. Jiang, J. Liu, J. Wang, J. S. Francisco, and X. C. Zeng, Proc. Natl. Acad. Sci. USA **116**, 16723 (2019).
[16] G. Algara-Siller, O. Lehtinen, F. C. Wang, R. R. Nair, U. Kaiser, H. A. Wu, A. K. Geim, and I. V. Grigorieva, Nature **519**, 443 (2015).
[17] R. Zangi and A. E. Mark, Phys. Rev. Lett. **91**, 025502 (2003).

[18] S. Han, M. Y. Choi, P. Kumar, and H. E. Stanley, Nat. Phys. **6**, 685 (2010).
[19] T. A. Pascal, C. P. Schwartz, K. V. Lawler, and D. Prendergast, J. Chem. Phys. **150**, 231101 (2019).
[20] Y. Zhu, F. Wang, J. Bai, X. C. Zeng, and H. Wu, ACS Nano **9**, 12197 (2015).
[21] R. R. Nair, H. A. Wu, P. N. Jayaram, I. V. Grigorieva, and A. K. Geim, Science **335**, 442 (2012).
[22] K. Gopinadhan, S. Hu, A. Esfandiar, M. Lozada-Hidalgo, F. C. Wang, Q. Yang, A. V. Tyurnina, A. Keerthi, B. Radha, and A. K. Geim, Science **363**, 145 (2019).
[23] A. Kalra, S. Garde, and G. Hummer, Proc. Natl. Acad. Sci. USA **100**, 10175 (2003).
[24] J. L. Abascal and C. Vega, J. Chem. Phys. **123**, 234505 (2005).
[25] Y. Huang, C. Zhu, L. Wang, X. Cao, Y. Su, X. Jiang, S. Meng, J. Zhao, and X. C. Zeng, Sci. Adv. **2**, e1501010 (2016).
[26] J. L. Aragones, M. M. Conde, E. G. Noya, and C. Vega, Phys. Chem. Chem. Phys. **11**, 543 (2009).
[27] T. Darden, D. York, and L. Pedersen, J. Chem. Phys. **98**, 10089 (1993).
[28] U. Essmann, L. Perera, M. L. Berkowitz, T. Darden, H. Lee, and L. G. Pedersen, J. Chem. Phys. **103**, 8577 (1995).
[29] G. Bussi, D. Donadio, and M. Parrinello, J. Chem. Phys. **126**, 014101 (2007).
[30] H. J. C. Berendsen, J. P. M. Postma, W. F. van Gunsteren, A. DiNola, and J. R. Haak, J. Chem. Phys. **81**, 3684 (1984).
[31] S. Nosé and M. Klein, Mol. Phys. **50**, 1055 (1983).
[32] M. Parrinello and A. Rahman, J. Appl. Phys. **52**, 7182 (1981).
[33] See Supplemental Material at http://link.aps.org/supplemental/10.1103/PhysRevB.101.165432 for the method of chemical potential calculations and additional figures.
[34] Z. Qiao, Y. Zhao, and Y. Q. Gao, J. Phys. Chem. Lett. **10**, 3115 (2019).
[35] W. G. Hoover, Phys. Rev. A **31**, 1695 (1985).
[36] S. Nosé, Mol. Phys. **52**, 255 (1984).
[37] D. Ben-Amotz, J. Phys.: Condens. Matter **28**, 414013 (2016).
[38] M. Kanduč and R. R. Netz, J. Chem. Phys. **146**, 164705 (2017).
[39] K. J. Strandburg, Rev. Mod. Phys. **60**, 161 (1988).
[40] N. D. Mermin, Phys. Rev. **176**, 250 (1968).
[41] D. Laage and J. T. Hynes, Science **311**, 832 (2006).
[42] D. Laage and J. T. Hynes, J. Phys. Chem. B **112**, 14230 (2008).
[43] M. A. Anisimov, M. Duška, F. Caupin, L. E. Amrhein, A. Rosenbaum, and R. J. Sadus, Phys. Rev. X **8**, 011004 (2018).
[44] M. Chen, R. Zhu, J. Zhu, and H. He, J. Phys. Chem. C **121**, 23752 (2017).
[45] P. Gallo, K. Amann-Winkel, C. A. Angell, M. A. Anisimov, F. Caupin, C. Chakravarty, E. Lascaris, T. Loerting, A. Z. Panagiotopoulos, J. Russo, J. A. Sellberg, H. E. Stanley, H. Tanaka, C. Vega, L. Xu, and L. G. M. Pettersson, Chem. Rev. **116**, 7463 (2016).
[46] J. C. Palmer, P. H. Poole, F. Sciortino, and P. G. Debenedetti, Chem. Rev. **118**, 9129 (2018).
[47] J. Russo and H. Tanaka, Nat. Commun. **5**, 3556 (2014).
[48] M. J. Cuthbertson and P. H. Poole, Phys. Rev. Lett. **106**, 115706 (2011).
[49] E. Shiratani and M. Sasai, J. Chem. Phys. **108**, 3264 (1998).
[50] N. J. Hestand and J. L. Skinner, J. Chem. Phys. **149**, 140901 (2018).
[51] J. Zubeltzu, F. Corsetti, M. V. Fernández-Serra, and E. Artacho, Phys. Rev. E **93**, 062137 (2016).
[52] T. Strässle, A. M. Saitta, Y. Le Godec, G. Hamel, S. Klotz, J. S. Loveday, and R. J. Nelmes, Phys. Rev. Lett. **96**, 067801 (2006).
[53] Y. Katayama, T. Hattori, H. Saitoh, T. Ikeda, K. Aoki, H. Fukui, and K. Funakoshi, Phys. Rev. B **81**, 014109 (2010).
[54] N. Giovambattista, P. J. Rossky, and P. G. Debenedetti, Phys. Rev. E **73**, 041604 (2006).
[55] H. Yoshida, V. Kaiser, B. Rotenberg, and L. Bocquet, Nat. Commun. **9**, 1496 (2018).
[56] Y. Leng and P. T. Cummings, J. Chem. Phys. **124**, 074711 (2006).
[57] A. S. de Wijn and L. G. M. Pettersson, Phys. Rev. B **95**, 165433 (2017).